Prediction of trailing-edge noise for separated turbulent boundary layers

Alexandre Suryadi

German Aerospace Center,
Institute of Aerodynamics and Flow Technology,
Lilienthalplatz 7, 38108 Braunschweig, Germany,
alexandre.suryadi@dlr.de

Abstract. This paper presents a semi-empirical low-order prediction of the trailing-edge noise of separated turbulent boundary layers. The prediction focuses on obtaining the low-frequency spectral peak of the far-field sound pressure level by modeling the measured wavenumber-frequency spectrum using regression analysis and integrating that spectrum in the manner of Howe's radiation model. Surface pressure fluctuations upstream of the trailing-edge of a DU96-W-180 blade section were measured using miniature pressure transducers, and the trailing-edge noise was measured using a directional microphone. The prediction showed that the far-field sound pressure level reached its maximum below the frequency limit of the directional microphone measurement, between 400 Hz - 500 Hz depending on the freestream velocity and the predicted spectrum varied between ± 0.5 dB given the inaccuracies of the regression model.

Keywords: prediction model, flow separation, trailing-edge noise

1 Introduction

The dynamics of the turbulent boundary layer (TBL) has been under investigation by many authors since its first conceptualization by Prandtl [1]. Under these investigations, the mean kinematics of the TBL studied are moving parallel to a surface or "attached" to the surface. In contrast, Simpson et al. [2] studied a "separated" TBL. Brooks et al. [3] developed spectral models of airfoil self-noise for different types of noise sources among them flow separation noise. Their model was developed to fit empirical datasets. Schüle and Rossignol, see [4] and [5], proposed a flow separation noise model based on the information of the boundary layer's velocity and turbulent normal stresses by using the so-called TNO surface pressure model, a popular model for the prediction of trailing-edge noise of an attached TBL (see [6] and [7]). Measurements of the trailing-edge noise (TEN) and the surface pressure upstream of the trailing-edge were performed at a DU96-W-180 blade section in the open jet Acoustic Wind-Tunnel Braunschweig, AWB [8]. Those measurements show that the TBL separates from the geometric angle of attack $\alpha = 8°$, corresponding to a 4.6° aerodynamic angle

of attack. While the flow separates, the lift curve continues to increase up to the point of stall (not measured). Thus, with unsteady upstream conditions, such as the atmospheric conditions experienced by wind turbine blades, intermittent flow separation may occur, produce more noise and increase the annoyance level of communities around a wind turbine.

Surface pressure measurements show that when the boundary layer separates, the surface pressure autospectral density changes in two ways compared to, for example, that of the canonical zero pressure gradient TBL. (i) An increase in the lower frequency region, $f < 1$ kHz and (ii) a steeper roll-off in level at mid to high frequencies [8]. The second trend is observable in the TEN measurements, using a directional microphone [5]. However, the directional microphone used in [5] is limited to 1 kHz $\leq f \leq$ 20 kHz due to its resolution and data correction procedure, such that the spectral peak of trend (i) was not captured in the far-field sound measurement.

A recent development describes the scaling of the mean velocity profile, U, and turbulent shear stress, $\overline{vv}$, for separated TBLs [9]. The scaling is based on the outer layer parameters: the boundary layer thickness, δ, and the local freestream velocity at $y = \delta$, U_e, and a non-dimensional maximum shear velocity $U_m = (\sqrt{Re_\delta}/U_e)\sqrt{\tau_m/\rho}$, where Re_δ is the Reynolds number based on U_e and δ, τ_m is the maximum viscous shear stress, and ρ is the density. This scaling, expressed in Eqs. (1) and (2), is also suitable to scale both the surface pressure integrated power spectrum and TEN sound pressure level (SPL) spectrum.

$$L'_{p,1/3} = L_{p,1/3} - 50\log(U_e/a_\infty) + 20\log(U_m) - 10\log(\delta/l_{ref}) \tag{1}$$

$$f^+ = \frac{f\delta}{U_e}\frac{1}{U_m^2} \tag{2}$$

The variables in Eqs. (1)-(2) are $L_{p,1/3}$: 1/3-octave band sound pressure level of far-field noise, $p_{ref} = 20\ \mu$Pa, a_∞: speed of sound, l_{ref}: reference length, 1 m. The two spectra (Figs. 7 and 8 in [9]) show good agreement with each other in the frequency domain for the lower, more interesting frequencies for separated TBL. The far-field noise and surface pressure are related according to Howe's radiation model for classical (attached TBL) trailing-edge noise. Howe's radiation model for an observer directly above or below the noise source is

$$S(\omega) = \frac{1}{4\pi R^2}\left(\frac{\omega L}{a_\infty}\right)\int_{-\infty}^{\infty}\frac{\Phi_{pp}(k_x, 0, \omega)}{(k_x - \omega/a_\infty)}\,\mathrm{d}k_x, \tag{3}$$

where ω is the radial frequency, R is the distance of the observer to the noise source, L is the length of the wetted span, a_∞ is the speed of sound, and $\phi_{pp}(k_x, k_z, \omega)$ is the wavenumber-frequency cross-spectrum where k_x and k_z are the wavenumbers in the streamwise and spanwise directions, respectively.

It is worth noting that the three-dimensionality of the separated turbulent boundary layer is observable using surface oil flow visualization that develops into "mushroom"-shaped structures. Schüle and Rossignol measured the boundary layer height near the trailing-edge of the DU96-W-180 airfoil [4] and showed that the boundary layer height weakly varies with the spanwise direction.

The goal of this study is the calculation of separated flow noise through the modeling of the cross-spectrum of the surface pressure fluctuation.

2 Experimental setup

All measurements were performed in the Acoustic Wind-Tunnel Braunschweig (AWB), an open jet wind tunnel with nozzle dimensions of 0.8 m wide and 1.2 m high. The maximum possible velocity is 65 m/s. The airfoil model, DU96-W-180, has a span length of 0.8 m and chord length of 0.3 m, and was mounted on wall extensions at either end of the nozzle width. Boundary layer fences 0.1 m away from these wall extensions are installed to limit the effect of the wall to the boundary layer development. The airfoil model was instrumented with ultra-miniature pressure sensors LQ-062-0.35 from Kulite semiconductors. From the manufacturer's description, these sensors have a typical natural frequency of 150 kHz. A high-pass filter with a cut-off frequency of 200 Hz filtered the voltages from the pressure sensors. These voltages were then amplified with a 250× gain before being converted to digital signal and stored. To reduce spatial attenuation these sensors were mounted under pinholes with a diameter of 0.5 mm ($d^+ = du_\tau/\nu = 29$ for $\alpha = 0°$ and $U = 60$ m/s). According to Gravante et al. [10], the value of $d^+ > 18$ will attenuate the spectral content in the dissipative range (zero pressure gradient TBL, $Re_\theta = 4972 - 7076$[1]), which is above the frequency range of interest of the present study. On the suction side of the airfoil model, eight sensors were installed along the streamwise direction and, unfortunately, only three along the spanwise direction were available. Measurements using each installation configuration were performed separately. Further description of the surface pressure sensor setup has been provided in Suryadi and Herr [8].

Scüle and Rossignol [5] documented the far-field noise of a DU96-W-180 at high angles of attack using a directional microphone. The directional microphone system consists of an elliptical reflector and a microphone. The elliptical reflector behaves like a mirror for sound waves. The sound waves travel to the inner surface of the elliptical disk and are reflected towards the near-focal point of the ellipse, where the microphone is mounted. Signals originating from the far-focal point of the ellipse that travel with the same travel length are in-phase and amplified at the microphone's position. Corrections of the output signal of the microphone consist of correction for gain and spatial resolution, correction of extraneous noise sources, and correction of the assumed model source. For the particular system in the AWB, the meaningful output is limited to a frequency range between 1 kHz and 20 kHz. For the fundamental of the directional microphone, the readers are directed to Sen [11] and for particularly the system in the AWB to Herr [12].

The turbulent boundary layers of the DU96-W-180 airfoil as mounted in the AWB separate when the geometric angle of attack, α is larger than 8°. For freestream velocity $U = 40$ m/s, 50 m/s, and 60 m/s, the pressure sensors measured the surface pressure fluctuations for $\alpha = 11°, 12°, 13°, 14°$ and 14.7°. Measurement data of the far-field noise are available for $\alpha = 11°, 13°$ and 14.7°.

[1] Reynolds number based on the momentum thickness

3 Result

Figure 1 is the normalized surface pressure autospectra for the sensor positioned closest, 13 mm upstream of the trailing edge. The normalization was given in [9] as

$$\Phi'_{pp}(f^+) = (U_e U_m^2/\rho^2 U_e^4 \delta)\Phi_{pp}(f) \tag{4}$$

$$f^+ = \frac{f\delta}{U_e}\frac{1}{U_m^2} \tag{5}$$

where $\Phi_{pp}(f)$ is the dimensional autospectral density, Φ'_{pp} is its non-dimensional form. The scaled autospectra show good agreement for $f^+ < 0.5$ for different αs and Us with exception at $\alpha = 14.7°$, where the scaled level is higher at $f^+ < 0.2$. This is possibly due to the angle $\alpha = 14.7°$ being very close to the stall angle that the TBL dynamics is no longer self-similar with the other, lesser αs.

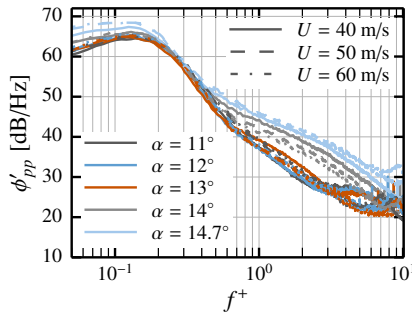

Fig. 1. (*Color online*) Surface pressure power spectral density for the pressure sensor 13 mm upstream of the trailing edge.

The coherency of the surface pressure signal is given as

$$\gamma(f, \boldsymbol{\xi}) = \frac{|\Phi_{pp}(f, \boldsymbol{\xi})|}{[\Phi_{pp}(f; \mathbf{x})\, \Phi_{pp}(f; \mathbf{x} + \boldsymbol{\xi})]^{1/2}}, \tag{6}$$

where $\Phi_{pp}(f, \boldsymbol{\xi})$ is the cross-spectral density function of $p(\mathbf{x})$ and $p(\mathbf{x} + \boldsymbol{\xi})$. The two surface pressure fluctuations have autospectra denoted as $\Phi_{pp}(f; \mathbf{x})$ and $\Phi_{pp}(f; \mathbf{x} + \boldsymbol{\xi})$, respectively. The vectorial notations $\mathbf{x}$ represents the spatial position of the sensor and $\boldsymbol{\xi}$ represents the distance between two sensors. The streamwise and spanwise distances of two sensors with respect to the one on the mid-span and closest to the trailing-edge are denoted as ξ and η, respectively.

Examples of the coherence spectra for streamwise and spanwise sensor separations for the measurement configuration $U = 60$ m/s and $\alpha = 13°$ are shown in Figs. 2(a) and (b), respectively. The dashed line in Fig. 2 represents the exponential decay of attached TBL. For separated flow, the coherency spectra are

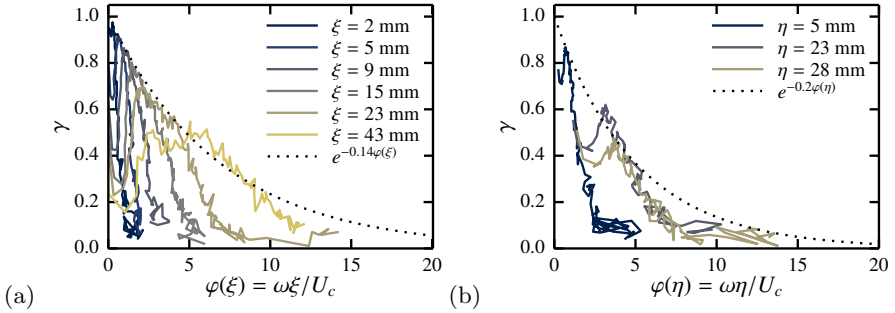

Fig. 2. (*Color online*) Coherence spectra of the surface pressure fluctuations. Dashed line indicate exponential decay. **(a)** Streamwise direction and **(b)** Spanwise direction.

distinctly different than for attached flow. Namely, after reaching its maximum, the coherence of separated TBL for a fixed, small value of ξ is lost abruptly instead of following the exponential decay of the attached TBL. Eventually, as ξ becomes larger the right-tail of the coherence spectrum follows the exponential decay. In Fig. 2(b) the phase angle $\varphi(\eta)$ was calculated using $U_c(f; \xi = 2 \text{ mm})$. The decay rate of the spanwise coherence spectra is less than the typical value for attached TBL, relating to the presence of large spanwise structure or the so-called "mushroom"-shaped structures.

4 Regression model of the coherency spectra

The surface pressure power spectral densities downstream of the separation point is approximately statistically homogeneous as shown in [8]. Hence, from Eq. (6) the space-frequency coherency spectrum can be written as

$$\Re\{\Phi_{pp}(f, \boldsymbol{\xi})\} \approx |\Phi_{pp}(f, \boldsymbol{\xi})| = \gamma(f, \boldsymbol{\xi})\Phi_{pp}(f; \mathbf{x}) = \gamma(f, \xi)\gamma(f, \eta)\Phi_{pp}(f; \mathbf{x}), \quad (7)$$

where $\Re$ denotes the real part of the cross-spectral density. With the scaled autospectral densities shown in Fig. 1, a regression model of $\Phi_{pp}(f; \mathbf{x})$ can be found, which for this purpose $\mathbf{x}$ is chosen to be the location of the sensor closest to trailing-edge (13 mm upstream of it). Thus, a regression model of γ is needed to represent the cross-spectral density function. The expression in Eq. (7) is the same as the one given by Corcos in [13].

A regression model of the coherency spectrum in the streamwise direction $\gamma(f, \xi)$ is formulated as

$$\gamma(f, \xi) = \gamma_{max}(\xi/\delta)\, \mathcal{G}(f^+, \sigma) \quad (8)$$

where γ_{max} is the coherence decay as a function of distance and $\mathcal{G}$ is the coherence shape function.

The coherence decay for ξ and η are shown in Fig. 3. The values of γ_{max} were taken from coherence spectra similar to Fig. 2 after applying a moving average

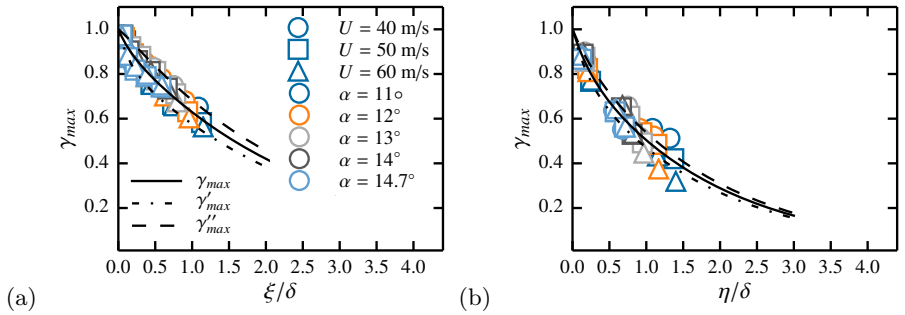

Fig. 3. (*Color online*) Decay of the coherence spectra as a function of distance **(a)** in the streamwise direction, and **(b)** in the spanwise direction.

with a uniform kernel. The regression model of the coherence decay along the streamwise direction is

$$\gamma_{max}(\xi) = ce^{-a\xi/\delta} + (1-c)e^{-b\xi/\delta}, \tag{9}$$

where a, b, and c are constants fitted to the data. The same expression is used for the decay in the spanwise direction with η replacing ξ. Using least-square approach, for the streamwise decay, $a = 0.404$, $b = 6.903$, and $c = 0.942$, and for the spanwise decay $a = 0.554$, $b = 4.662$, and $c = 0.875$, where b contributes to the steep decay for small sensor separation distances. Equation (9) is shown in Fig. 3 as a black solid line. The black dash-dot and dashed lines indicate the spread of the data that is represented by Eq. (9) and $c' = c - 0.06$ and $c'' = c + 0.06$.

The coherence shape function $\mathcal{G}(f^+, \sigma)$ is the coherence spectrum normalized by γ_{max}. Streamwise and spanwise coherence shape functions are shown in Figs. 4 and 5, respectively, for selected values of ξ and η. Due to smaller γ_{max} at large sensor separation distance, the spread of the coherence values increases. A combination of U and α is shown, where the shape of the markers represents U and the line colors represent α. The black solid lines in Figs. 4 and 5 are the coherence shape function defined as

$$\mathcal{G}(f^+, \sigma) = \frac{\gamma}{\gamma_{max}} = [1 - e^{-f^+/\tau}]e^{-(f^+ - f_0^+)^2/(2\sigma^2)} \tag{10}$$

where the first factor, $1-e^{-f^+/\tau}$, is the coherence at low-frequency with $\tau = 0.02$, given arbitrarily. The reason that the $1 - e$ factor is included is to reduce the coherence to zero at $f^+ \propto f = 0$, because $f = 0$ implies coherence of two signals separated by a very large time step that they are no longer coherent or correlated. The second factor is a Gaussian curve, where σ, typically the standard deviation, denotes the size of the bell curve and $f_0^+ = 0.15$ is the normalized frequency of the peak of the power spectral densities (see Fig. 1). The value of σ is expressed for each direction as

$$\sigma(\xi) = 0.1723\xi^{-0.1} \text{ and } \sigma(\eta) = 0.0768\eta^{-0.25} \tag{11}$$

with ξ and η given in their dimensional values. However, because γ/γ_{max} is in the f^+ domain, it is reasoned that $\sigma(\xi)$ and $\sigma(\eta)$ also belong to the f^+ domain. The dashed-dot line in the same figures are lines drawn by Eq. (10) with $\sigma' = \sigma - 0.06$ leading to $\mathcal{G}'$ and the dashed line is for $\sigma'' = \sigma + 0.06$ leading to $\mathcal{G}''$. These two lines quantify the spread of the empirical data. These and the same lines in Fig. 3 will be used later in the study for error analysis.

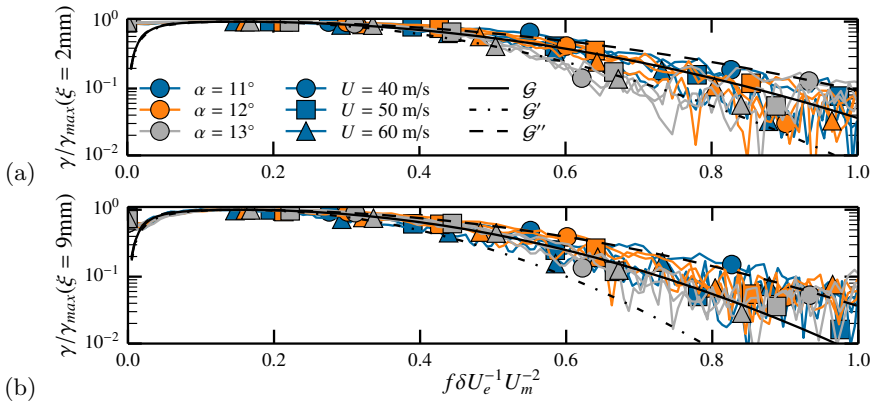

Fig. 4. (*Color online*) Example of coherence shape function of two sensors ξ apart. For legend explanation see text. **(a)** $\xi = 2$ mm, and **(b)** $\xi = 9$ mm.

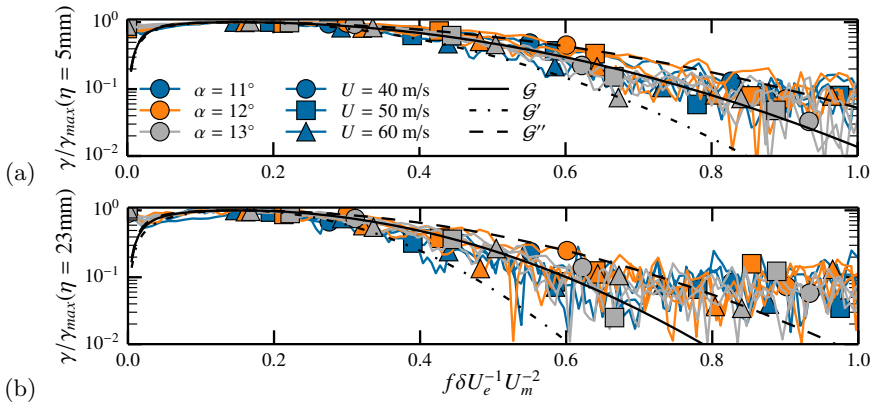

Fig. 5. (*Color online*) Example of coherence shape function of two sensors η apart. For legend explanation see text. **(a)** $\eta = 5$ mm, and **(b)** $\eta = 23$ mm.

Given the reason above, the wavenumber-frequency spectrum model is expressed in Eq. (12), where $\mathcal{F}_{\boldsymbol{\xi}}$ is the spatial Fourier transform, $\mathbf{k} = (k_x, k_z)$ is

the wavenumber vector with elements in the streamwise and spanwise direction, respectively, and $\hat{\Phi}_{pp}(f^+)$ is the regression function of the normalized surface pressure autospectrum.

$$\begin{aligned}\hat{\Phi}_{pp}(f,\mathbf{k}) &= \mathcal{F}_{\boldsymbol{\xi}}\{\Phi_{pp}(f,\boldsymbol{\xi})\} \\ &= \mathcal{F}_{\xi}\{\gamma_{max}(\xi)\}\mathcal{G}_{\xi}(f^+,\sigma(\xi))\,\mathcal{F}_{\eta}\{\gamma_{max}(\eta)\}\mathcal{G}_{\eta}(f^+,\sigma(\eta)) \\ &\quad \hat{\Phi}_{pp}(f^+)\frac{(1/2\,\rho U_c^2)^2\delta}{U_e U_m^2}\end{aligned} \tag{12}$$

The Fourier transform of $\gamma_{max}(\xi)$ is

$$\mathcal{F}_{\xi}\{\gamma_{max}(\xi)\} = \frac{2}{\sqrt{2\pi}}\left[\frac{ac\delta}{a^2+k_x^2\delta^2} + \frac{b(1-c)\delta}{b^2+k_x^2\delta^2}\right] \tag{13}$$

and similarly for the spanwise directions by replacing ξ for η and k_x for k_z. The values of a, b, c previously mentioned apply to Eq. (13) for the respective direction of coherence decay. Because the far-field sound radiation in Eq. (3) requires the integration of the wavenumber-frequency spectra with $k_z = 0$, the spanwise coherence is simplified into

$$\mathcal{F}_{\eta}\{\gamma_{max}(\eta)\} = \frac{2}{\sqrt{2\pi}}\left[\frac{c\delta}{a} + \frac{(1-c)\delta}{b}\right] \tag{14}$$

Low order prediction of the surface pressure autospectra and the far-field sound, as denoted by lines, is compared with the measurements, as denoted by markers in Fig. 6. Each of the predicted autospectrum in Fig. 6(a) is a product of the integration of $\Phi_{pp}(k_x, \eta = 0, f)$ with respect to k_x, where the integrand is equal to $\mathcal{F}\{\gamma_{max}(\xi)\}\mathcal{G}_{\xi}\hat{\Phi}_{pp} = \int_{-\infty}^{\infty}\Phi_{pp}(k_x,k_z,f)\,\mathrm{d}k_z$. The integration of the autospectrum was done this way to avoid an oversized calculation matrix. The predictions produce curves in the low-frequency range where the sound pressure maxima are located, where the energy content of the surface pressure fluctuations is also the strongest. The reason the spectral peaks are predominantly at low frequency was explained by Simpson et al. [14], who measured the velocity within a separated TBL. They found that downstream of flow separation, turbulent production terms near the wall are smaller compared to attached TBL and turbulence production in the outer layer supplies the turbulent energy near the wall by turbulent diffusion.

Comparison of the prediction of the trailing-edge noise in Fig. 6(b) with that given in [5] reveal that the spectral peaks derived by the present model are between 5 dB to 10 dB higher and the frequency of the spectral peaks are 200 Hz - 300 Hz larger depending on the value of α. Furthermore, the calculation of the TEN does not assume boundary layer properties that originate from attached TBL.

5 Error analysis

The robustness of the regression model is examined by substituting the values c in Eq. (9) and σ in Eq. (10) so that γ_{max} and $\mathcal{G}$ encompasses the spread

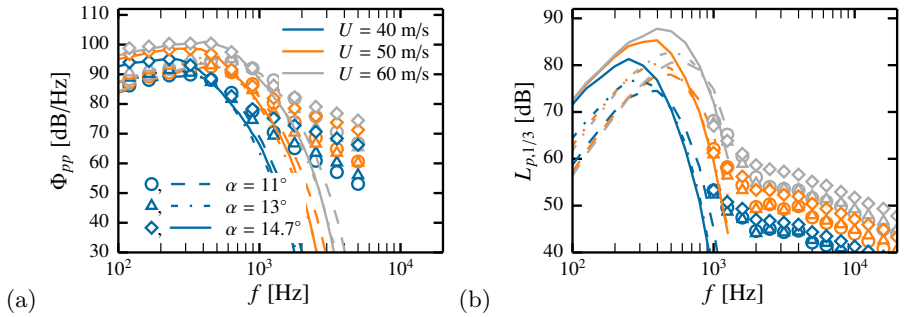

Fig. 6. (*Color online*) Spectral predictions based on the regression model, Eq. (12). **(a)** reconstructed surface pressure autospectra (smaller number of markers are shown for clarity) and **(b)** far-field sound pressure level spectra.

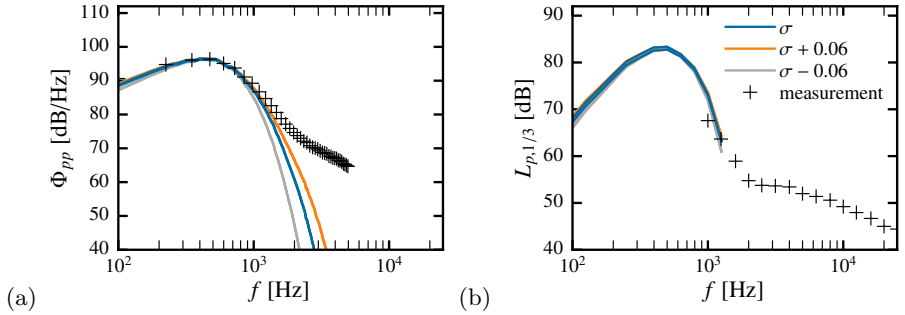

Fig. 7. (*Color online*) Error analysis for configuration $U = 60$ m/s and $\alpha = 13°$. **(a)** surface pressure autospectra (smaller number of markers are shown for clarity) and **(b)** far-field sound pressure level spectra.

of the empirical data. For γ_{max}, an addition of -0.06 to c leads to the curve γ'_{max} and +0.06 leads to γ''_{max} in Fig. 3. The spread of the empirical coherence shape function is bounded by the dashed lines in Figs. 4 and 5, where $\mathcal{G}' = \mathcal{G}(f^+, \sigma - 0.06)$ and $\mathcal{G}' = \mathcal{G}(f^+, \sigma + 0.06)$ for the respective σ of either direction. The inaccuracies of the regression model are shown in Fig. 7 for the measurement configuration $U = 60$ m/s and $\alpha = 13°$. It shows that the spectral prediction is weakly dependent with c and more strongly with σ. In fact lines due to the variation of c are plotted in Fig. 7, but they overlap each other. Despite the variation in the coherence shape function, the spread of the sound pressure level is within ±0.5 dB.

6 Conclusion

This paper presents a model to calculate the far-field sound of turbulent flow separation. The model was derived from empirical data of surface pressure fluctuations near the trailing edge. It was shown that the model reconstructed the

surface pressure autospectrum in the low-frequency region, which resulted in a low-frequency spectrum for the far-field noise that complements the measurement result, which is limited to frequencies above 1 kHz. Variations in the regression model result in variations in the far-field sound of ±0.5 dB.

GE Wind Energy GmbH sponsored the present study between 2012 and 2015.

References

1. Prandtl, L.: Zur berechnung der grenzschichten. ZAMM-Journal of Applied Mathematics and Mechanics/Zeitschrift für Angewandte Mathematik und Mechanik, 18(1), pp. 77–82 (1938). doi:10.1002/zamm.19380180111
2. Simpson, R.L., Ghodbane, M., McGrath, B.E.: Surface pressure fluctuations in a separating turbulent boundary layer. J. Fluid Mech. 177, pp. 167–186 (1987). doi:10.1017/S0022112087000909
3. Brooks, T.F., Pope, S., Marcolini, M.A.: Airfoil self-noise and prediction. Technical Report, NASA-RP-1218 (1989).
4. Schüle, C.Y., Rossignol, K.S.:A separated flow model for semi-empirical prediction of trailing edge noise. In: Dillman, A., et al. (eds.) New Results in Numerical and Experimental Fluid Mechanics IX, vol 124, pp. 639–647, Springer, Heidelberg (2014). doi:10.1007/978-3-319-03158-3
5. Schüle, C.Y., Rossignol, K.S.: Trailing-edge noise modeling and validation for separated flow conditions. In: 19th AIAA/CEAS Aeroacoustics Conference, AIAA 2013-2008 (2013). doi:10.2514/6.2013-2008
6. Herr, M., Kamruzzaman, M.: Benchmarking of trailing edge noise computations - outcome of the BANC-II workshop. In: 19th AIAA/CEAS Aeroacoustics Conference, AIAA 2013-2123 (2013). doi:10.2514/6.2013-2123
7. Herr, M., Bahr, C.J., Kamruzzaman, M.: Broadband trailing-edge noise predictions - overview of BANC-III results. In: 21st AIAA/CEAS Aeroacoustics Conference, AIAA 2015-2847 (2014). doi:10.2514/6.2015-2847
8. Suryadi, A., Herr, M.: Wall pressure spectra on a DU96-W-180 profile from low to pre-stall angles of attack. In: 21st AIAA/CEAS Aeroacoustics Conference, AIAA 2015-2688 (2015). doi:10.2514/6.2015-2688
9. Suryadi, A.: Kinematic and acoustic similarities of separated turbulent boundary layers. In: 24th AIAA/CEAS Aeroacoustics Conference, AIAA 2018-3937 (2018). doi:10.2514/6.2018-3937
10. Gravante, S.P., Naguib, A.M., Wark, C.E., Nagib, H.M.: Characterization of the pressure fluctuations under a fully developed turbulent boundary layer. AIAA J. 36(10), pp. 1808–1816 (1998). doi:10.2514/2.296
11. Sen, R.: Interpretation of acoustic source maps made with an elliptic-mirror directional microphone system. In: Aeroacoustics Conference, AIAA 1996-1712 (1996). doi:10.2514/6.1996-1712
12. Herr, M.: Trailing-edge noise: reduction concepts and scaling laws. PhD dissertation, Technical University Braunschweig (2013). ISSN1434-8454
13. Corcos, G.M.: The structure of the turbulent pressure field in boundary-layer flows. J. Fluid Mech. 18(3), pp. 353–378 (1964).doi:10.1017/S002211206400026X
14. Simpson, R.L., Chew, Y.T., Shivaprasad, B.G.: The structure of a separating turbulent boundary layer. Part 2. Higher-order turbulence results. J. Fluid Mech. 113, pp. 53–73 (1981).doi:10.1017/S0022112081003406